Marine Structures 90 (2023) 103426

Contents lists available at ScienceDirect

Marine Structures

journal homepage: www.elsevier.com/locate/marstruc

Design and model test of a soft-connected lattice-structured floating solar photovoltaic concept for harsh offshore conditions

Zhiyu Jiang [a], Jian Dai [b,*], Simone Saettone [c], Glenn Tørå [d], Zhao He [a,e], Musa Bashir [f], Antonio Souto-Iglesias [c]

[a] Department of Engineering Sciences, University of Agder, N-4879, Grimstad, Norway
[b] Department of Built Environment, Oslo Metropolitan University, Oslo, 0166, Norway
[c] CEHINAV, ETSIN, Universidad Politécnica de Madrid, Madrid, Spain
[d] cDynamics AS, N-4633, Kristiansand, Norway
[e] Aker Solutions ASA, N-1364, Fornebu, Norway
[f] Liverpool Logistics, Offshore and Marine (LOOM) Research Institute, Liverpool John Moores University, Liverpool, UK

ARTICLE INFO

Keywords:
Floating photovoltaic technology
Offshore environment
Conceptual design
Soft connection
Model test
Motion performance

ABSTRACT

Various types of floating solar photovoltaic (FPV) devices have been previously proposed, designed and constructed with applications primarily limited to onshore water bodies or near-shore regions with benign environmental conditions. This paper proposes a novel FPV concept which can survive harsh environmental conditions with extreme wave heights above 10 m. This concept uses standardised lightweight semi-submersible floats made of circular materials as individual modules. The floating modules are soft connected with ropes to form an FPV array. We first present the conceptual design of the floats and the connection systems, including hydrostatic, hydrodynamic, and structural assessments of the floats. To verify the motion response performance, we carried out 1:60 scaled model tests for a 2 by 3 array under regular and irregular wave conditions. From the time series and response spectra, the motion characteristics of the array and the mooring responses are analysed in detail. The proposed concept exhibits excellent performances in terms of modular motions with limited wave overtopping and no contact is observed between adjacent modules under the extreme wave conditions. The findings of this study can serve as a valuable reference to developing reliable and cost-effective FPV technologies for offshore conditions.

1. Introduction

The global energy demand has been rising steadily. In one estimate [1], the total world energy consumption is expected to increase by 48% between 2012 and 2040. Renewables account for a rising share of the world's total electricity supply, and the energy resources of hydroelectric, wind, and solar are expected to play a dominant role by 2040.

Solar is the fastest-growing form of renewable energy with a net energy generation increase of 8.3% per year as of 2016.

Abbreviations: FPV, floating photovoltaic; HDPE, high-density polyethylene; LCOE, levelised cost of energy; MW, megawatt; RAO, response amplitude operator; TRL, technology readiness level.

* Corresponding author.
E-mail addresses: zhiyu.jiang@uia.no (Z. Jiang), jiandai@oslomet.no (J. Dai).

https://doi.org/10.1016/j.marstruc.2023.103426
Received 6 July 2022; Received in revised form 21 March 2023; Accepted 27 March 2023
0951-8339/© 2023 The Authors. Published by Elsevier Ltd. This is an open access article under the CC BY-NC-ND license (http://creativecommons.org/licenses/by-nc-nd/4.0/).

Photovoltaic (PV) systems are the most common type of applications which directly convert sunlight into electricity via electronic devices. So far, utility-scale PV systems of megawatt (MW) power capacity have been successfully applied to roof tops, ground-mounted plants, and floating water bodies like reservoirs [2].

A floating PV (FPV) system typically consists of floating structures, connection systems, mooring and anchoring, inverters, under- or above-water cabling, and solar panels with their support structures. Although the development of FPV technologies has evolved primarily in the past decade, most applications are limited to only freshwater bodies or nearshore sheltered areas with benign water environments [3]. For such applications, the environmental load effects, *e.g.,* from waves and currents, are rather small, and the maintenance accessibility is good. As the manufacturing, installation and maintenance costs are of major concerns to the FPV industry, the trend is to adopt standardised floating modules made of lightweight materials like high-density polyethylene (HDPE) to house PV panels and to use semi-rigid or flexible connectors to connect the floating modules. Case studies of such FPV systems can be found in the 1-MW FPV testbed at Tengeh Reservoir in Singapore [2,4].

Owing to the limited space to deploy large scale solar farms onshore, like the offshore wind industry, the FPV industry is expected to experience a transition from nearshore to offshore applications, moving from shallow to immediate or deep water. Offshore environments, characterised by salty water and strong currents, waves, and wind, pose significant technical and economic challenges to the design of FPV structures [5]. The technical challenges include material durability, recyclability, corrosion resistance, structural safety, and remote operation and maintenance, to name a few. The economic challenges primarily concern the levelised cost of energy (LCOE) of the offshore FPV systems in the context of nearshore applications or other types of renewable energy devices.

As shown in Table 1, many FPV concepts with potential for offshore applications have been proposed. Due to the proprietary nature of commercial activities, limited information is available, and the listed Technology Readiness Level (TRL) and survival environments only serve as estimates with uncertainties. Three concepts, *i.e.,* Swimsol, Heliofloat and SolarDuck consider large floats and high technical complexities are expected. Most concepts except the new design to be presented in this paper use mechanical hinge connectors to connect the floating modules. Out of the nine concepts, only the Moss Maritime, HelioRec and the present concept have been tested or have ongoing test campaigns under offshore conditions with rough seas. Additionally, the Dutch "solar-at-sea" project is not listed here because of missing technical details. This Dutch project has prototypes that can survive 10-m waves and have a reported LCOE of 354 €/MWh [6]. Currently, there is a strong demand for developing technically feasible, economically viable, and environmentally friendly FPV technologies for offshore conditions.

This paper systematically presents the research and development efforts behind an innovative and promising concept with material recyclability, lightweight modular structure, and excellent motion performance under extreme waves. As the concept is new, the focus of this paper is laid on the conceptual development and motion performance of a small array. It must be emphasised that topics like structural optimisation, mooring and anchor system design, material degradation and recyclability, array installation, operation and maintenance, energy performance, and lifecycle assessment deserve dedicated studies and are out of the scope of this study.

This paper is arranged as follows. Section 2 describes the conceptual development with a focus on the float and the connection system. Section 3 describes the model tests of a scaled FPV array (2 × 3) carried out at UP Madrid in October 2021. Section 4 presents the model test results. Here, selected numerical studies by using OrcaFlex were also conducted, and a comparison is made between the numerical and experimental results for selected regular wave conditions. Section 5 presents the uncertainty analysis of the model tests. Finally, concluding remarks are drawn in Section 6.

2. The soft-connected semi-submersible floating solar farm concept

2.1. General

In this section, we introduce the concept development of an innovative FPV farm and show fundamental hydrostatic, hydrodynamic, and hydroelastic calculations for the selected float and material. Note that details of the design including the float geometry and material composition are out of the scope of this paper and will be reported in a future study.

Table 1
Summary of selected marine FPV technologies for offshore applications, collected from the public domain.

Technology	Country/year	Selected technical features
T3F-PV [7]	Canada/2013	Floating thin film PV panels with mechanical coupling; prototype tested in a pond. TRL>4.
Swimsol [8]	Maldives/2014	Large semi-submersible floater made of styrofoam and aluminium frame; prototype tested in Maldives. TRL>4. Survival environment: Hs = 1.5–2 m.
SUNdy	Norway/2012	Hexagonal array with thin-film PV panels. No prototypes presented. TRL:1-2
Heliofloat [9]	Austria/2016	Large floating platforms (60 × 60 m) that hover above the water on air cushions. TRL: 4–5.
Ocean Sun [10]	Norway/2018	Large cylindrical floaters with PV modules supported by thin hydroelastic membranes. TRL>7.
Moss Maritime [11]; [12]	Norway/2018	Floating platform (10 × 10 m) connected by cubic floaters made of steel framed structure. Resilience test planned off the Frøya island. TRL: 3. Survival environment: Hs = 3–4 m.
SolarDuck	The Netherlands/ 2021	Large triangular platform supported on aluminium legs. TRL: 3.
HelioRec [13]	France/2020	Floating platform connected by cubic floaters connected by flexible mechanical connectors. Resilience test in France. TRL: 3.
Present concept	Norway/2021	Floats made of porous pontoons and cylinders, connected by ropes. Resilience test in Spain. TRL: 3. Survival environment: Hs = 10 m.

2.2. Technology maturity

The design concept is inspired by the Singaporean 5-MW coastal FPV project off the coast of Woodlands with mechanical connection, the criss-crossed nets of Norwegian fish cages, and the cost-effective floating wind turbine concept TetraSpar [14]. Unlike traditional FPVs which use rigid or semi-rigid connections, the present design has a lattice of soft-connected floats supporting PV panels. This configuration allows the modules to have large deformations in extreme seas. After technical assessments and four roundtable discussions with industrial partners and disciplinary experts, we determined the basic design of the individual modules and the form of the connection system. Then, calculations were conducted to obtain the overall dimensions of the modules and physical properties, *e.g.,* natural periods and hydrostatic stability of the concept. TRL 3 (experimental proof of concept) was established after

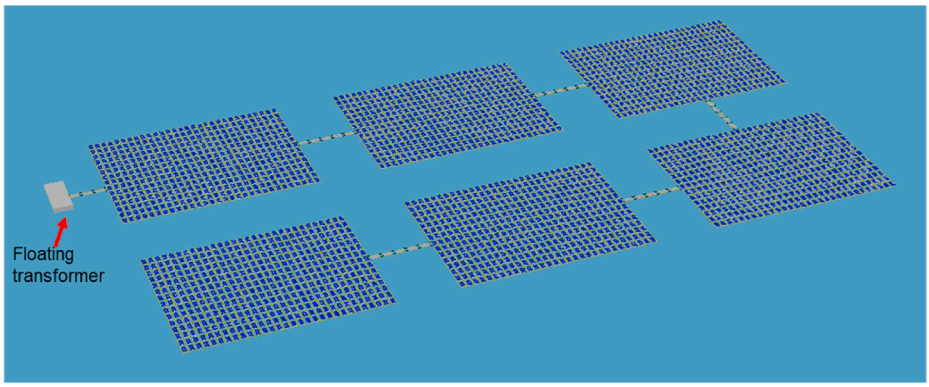

(a)

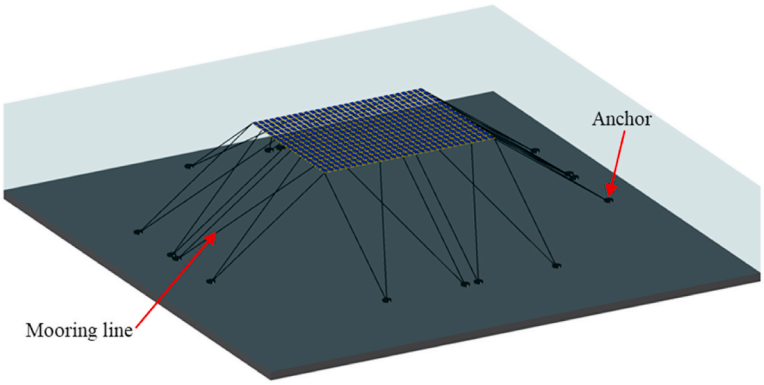

(b)

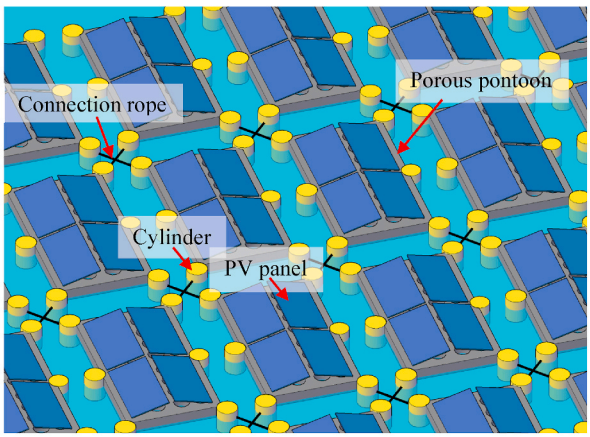

(c)

Fig. 1. Illustration of 6 MW FPV farm and structural components: (a) global view of FPV farm, (b) solar array, and (c) connected floats.

wave tank tests were carried out to verify the survivability of an FPV array under extreme wave conditions.

2.3. Design challenges

The design principles for the structural system (floats, support structures for solar panels, and moorings) of FPVs are like those of other offshore structures [15]. According to the DNV recommended practice [5], the design should target at an annual failure probability of 10^{-4} with the consequence category 1 (failure unlikely to lead to unacceptable consequences). In addition, the recommended practice also requires modelling of extreme environmental conditions and assessment of global loads and dynamic responses. The environmental loads include wave, wind, current, ice, and seismic effects. As the FPV industry is at a nascent stage, no specifically calibrated partial safety factors for load and resistance can be applied to structural design of FPV systems in terms of the ultimate, fatigue, and accidental limit states. Those factors should be calibrated by means of structural reliability methods [16]. A calibration process of other types of offshore structures can be found in Ref. [17].

For offshore FPVs, the floats, materials, and moorings will endure the stress cycles due to environmental actions. Although no site-specific metocean conditions are considered in this study, it is expected that the key structural components (floats, rope connections, mooring lines) of an FPV array should remain intact under survival extreme environmental conditions typical of the North Sea, *e.g.,* wave height >14 m, wind speed >25 m/s, and current speed >1.2 m/s. Thus, the first challenge is to design a structural system with good durability throughout the design lifetime, *e.g.,* 25 years. At the same time, the LCOE is a driving factor behind any types of novel renewable energy devices. So, another challenge is to develop the structural system with low cost such that the concept is cost-effective compared to other concepts. Overall, to tackle these challenges, a new "mindset" is required when designing the FPV structural system to achieve the required durability while maintaining cost-effectiveness.

2.4. Conceptual design

For the offshore FPV, the design rationale is built upon three fundamental principles: (1) minimal environmental loads, (2) low cost, and (3) circularity. The first principle leads to a lightweight float design and a unique, soft connection system (with ropes). By doing so, the lattice-shaped FPV array follows the wave envelopes in a storm condition. The second principle dictates that the components (*e.g.,* cylinders and porous pontoons) adopt a simple configuration that can be produced, transported, assembled, installed, maintained and repaired at low costs. The third principle is reflected through the choice of recycled fibres for material components and integration of the FPV system with low-carbon footprint technologies. Note that this aspect is not addressed in this study, but it is envisaged that composites from recycled fibre materials and HDPE materials will be applied to the floats.

Fig. 1 shows an FPV farm with all essential components of the FPV arrays, floating linkage, floating transformer, connections, and mooring systems. Each FPV array has a power generation capacity of 1 MW and is composed of many standard floats, soft-connected using ropes to mitigate fatigue issues. Both the porous pontoon and the cylinders are watertight and hollow inside and are made of durable circular materials composed of fibre-reinforced HDPE for mass fabrication, and storage and transportation using standard containers. Each float can house four standard PV panels arranged in a dual-pitch configuration to mitigate the shading effect of one panel to its neighbouring panels and reduce the wind loads with a streamlined profile. They are lightweight, free-floating, and self-stabilising, thus alleviating the wave loads through motions following the waves. The arrays are individually held in place by using a low-carbon mooring system equipped with tethers comprising both progressive elastomeric elements with synthetic ropes [18]. Moreover, splitters are employed to connect one mooring tether to multiple floating modules to ensure sufficient structural capacity of the tethering point on the floating modules while avoiding the need for many mooring lines that complicate onsite marine operations. The FPV arrays are electrically linked to each other via the floating linkage formed by the standard floats. The generated power will be transmitted to a floating transformer stationed on the side for easy access via boats. The concept features a modular design with standardised components for easy fabrication and connection to form an FPV farm of various desirable shapes and sizes in a Lego-set fashion.

2.4.1. Float design

Marine structures in offshore locations are exposed to undesirable environmental effects such as repetitive wave forcing, UV degradation, chloride attack, temperature variation, and marine growth. The float design must take the material selection and design must reflect on these design requirements while considering fabricability, circularity and sustainability. To address this challenge, a lightweight, durable, and cost-effective material solution is proposed for harvesting solar energy from harsh offshore environment and will leverage the previous experience in developing very large FPV farms in coastal marine conditions. The HDPE material is chosen to the base material for developing new composite materials in view of its material strength and durability in marine environments. To improve the material and structural performance, recyclable and corrosion-free fibres like carbon fibres are proposed as reinforcement to strengthen the mechanical properties of the composite material. Different fibre volumes may be applied, depending on the structural requirements of the floats at various locations. The structural performance of HDPE material and its circularity for sustainability can be strengthened by mixing it with corrosion-free fibres.

As shown in Fig. 1, each standard float comprises a porous pontoon and six cylinders, both made of composite materials. The floats are designed with a low freeboard to attract small wind loads and to achieve a good cooling effect due to proximity to the water surface. The overall planar dimension of a float is on the order of 4.7 m in length and 2.9 m in width. Note that the detailed dimensions need to be calculated and validated through comprehensive engineering design, which is outside the scope of this study. Each porous pontoon is designed to accommodate four PV panels of standard sizes. The porosity is designed to improve the air circulation between the solar

panels and the water surface. The bottom of the porous pontoon is designed to merely cover the water surface. This, in combination with the pontoon dimensions and characteristics of the typical ocean waves, reduces undesirable water entry and water exit type loads affecting the pontoon. The cut-outs also help dissipate the wave energy. Both the cylinders and porous pontoon are hollow inside so that they are lightweight and buoyant. They are made of the above-mentioned innovative circular composite material and can be mass fabricated, stored and transported using standard containers. When they are assembled and towed to the site, the cylinders are the main buoyancy provider with a small water plane area, thus reducing the hydrodynamic actions.

2.4.2. Connection, mooring and anchor systems

Float to float connections are critical components in modularised floating structures and must be designed with adequate strength to resist environmental loads. At the same time, the connections shall also be designed with a weaker strength than the floating modules such that they may fail in an extreme event before any occurrences of a catastrophic damage of the system. Moreover, it is appropriate to design connectors that do not transmit bending moments as the wave-induced forces and movements are expected to be large in an offshore condition. To address this challenge, the use of soft connections by using elastic ropes is proposed as shown in Fig. 1. Such connection systems utilise non compressive members to tie the floating modules together and the only action effect lies in the axial force. Compared with other types of connection systems for marine structures, rope connections, when properly designed, attract lower connection forces and are less prone to fatigue concerns. Such a compliant rope connection system has been successfully applied to floating wind farms [19] and floating hydrocarbon storage tanks [20].

The FPV arrays are designed to move freely in the vertical direction following the waves. To keep such a huge and complex system horizontally in position under adverse offshore environmental conditions, the design of the anchoring and mooring system must consider the actions arising from combined wave, wind, and current loads. Furthermore, the vertical load components to be developed in the anchoring and mooring system due to wave loads and tide-induced water surface elevation change will act as a burden to the proposed floats as they are designed with a light carrying capacity. This is because the floats to house the solar panels are designed to be lightweight with a small draft such that they can easily follow the water surface wave motions and thereby avoiding undesirably high wave loads. Consequently, they may not have sufficient buoyancy to counteract the large vertical mooring loads arising from water waves and tidal variations. To address this challenge, detailed design and analysis of the mooring system must be carried out for a utility-scale array considering site-specific conditions like water depth, metocean conditions, and bathymetry. For water depth of more than 150 m, semi-taut synthetic arrangements with polyester ropes can be considered. Furthermore, a mooring load decomposition is achieved by employing floating buoyancy compensation systems attached to the tethers, leaving only a horizontal force to be transmitted to the FPV modules.

The mooring lines are anchored to the seabed via the installation of a range of direct embedment (drilled) anchor types for various seabed geotechnical conditions, from sand to hard rock, using subsea anchor installation ROVs. This approach negates the requirement for diver operation and opens up the opportunity to deploy FPVs in water depths beyond diver constraints.

2.4.3. Performance evaluation

The hydrostatic, hydrodynamic, and hydroelastic performance of the proposed standard float is evaluated before the detailed experimental model testing. The reinforced HDPE is assumed to have a composite density of 1300 kg and an average of 5 mm thickness for both the porous pontoon and the cylinders. For the porous pontoon, the porosity ratio is taken as 0.25. The total weights of two loading scenarios, namely, (a) a single standard float carrying 4 solar panels of 40 kg each and (b) a float carrying 4 solar panels and one maintenance personnel of 85 kg at the centre are approximately 535 kg and 620 kg, respectively. These correspond to the conditions that (a) the buoyancy is provided by the cylinders with a draft of 0.48 m and the bottom of the porous pontoon is just covering the free surface, and (b) the buoyancy is provided by both the cylinders and the porous pontoon with a draft of 0.45 m, respectively. Note that the first condition refers to the normal unmanned operational state with reduced wave impinging and impact forces. The dry draft when the maintenance personnel is standing at the far end of the porous pontoon is 0.25 m. The lowest initial metacentric heights of a standard float carrying four solar panels with and without a maintenance personnel are 11.02 m and 13.37 m, respectively, which are deemed sufficient.

Next, the heave natural period is estimated of an unmoored standard float in operational condition. Under such a situation, the majority of buoyancy is provided by the water displacement from the cylinders and the bottom surface of the porous pontoon is just covering the water surface. As such, both the cylinders and the porous potoon are accounted for when estimating the heave natural period. This can be calculated by

$$T_{n3} = 2\pi\left(\frac{M + A_{33}}{\rho g A_w}\right)^{\frac{1}{2}} \tag{1}$$

where M is the structural mass of the float, A_{33} is the added mass in heave, and A_w is the waterplane area.

For the cylinders, the added mass in heave can be estimated by

$$A_{33} = \left[1 + \sqrt{\frac{1-\lambda^2}{2(1+\lambda^2)}}\right] \bullet A_{330} \tag{2}$$

$$\lambda = \frac{\sqrt{A_p}}{h + \sqrt{A_p}} \tag{3}$$

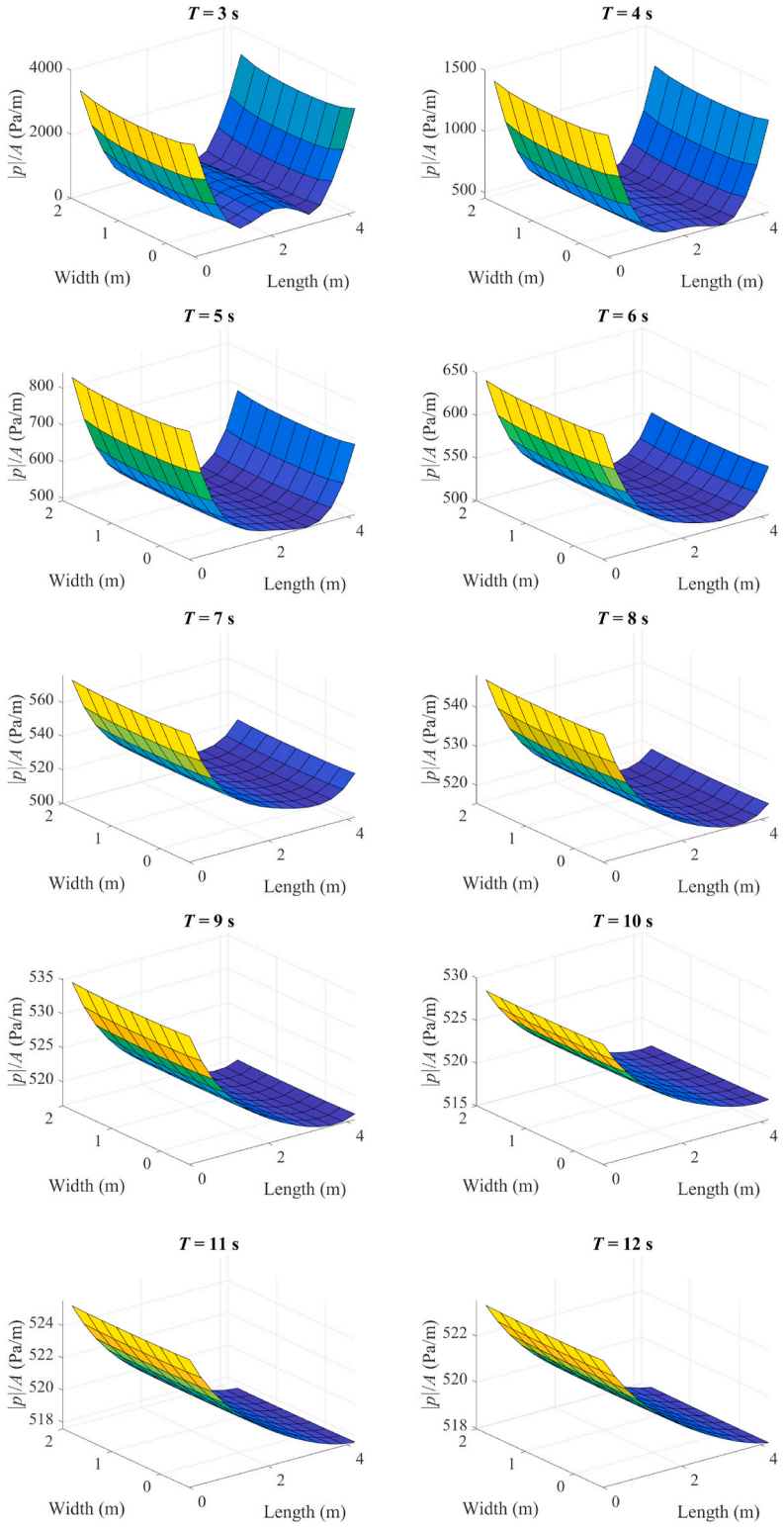

Fig. 2. Hydrodynamic pressure amplitude on a single standard float.

where A_{330} is the added mass for a flat plate with a shape equal to the horizontal projected area of the object; h is the height of the object, A_p is the area of submerged part of object projected on a horizontal plane.

For the porous pontoon with a porosity ratio of 0.25, the effect of perforation on the added mass may roughly be estimated by

$$A_{33} = A_{33s} \bullet \left(0.7 + 0.3 \bullet cos\left[\frac{\pi \bullet (p-5)}{34}\right]\right), \text{if } 5 < p < 34 \tag{4}$$

where A_{33s} is the solid added mass for a rectangular plate, and p is the porosity ratio. Eqs. (2)–(4) are simplified expressions from Ref. [21]. As these equations are derived from potential flow-based numerical simulations, computational fluid dynamics analysis or model tests are recommended if more accurate estimations are needed.

The porous pontoon is just slightly above the free surface in calm water during unmanned operations. Therefore, the influence of the submergence of the porous pontoon must be considered. According to Eq. (1), the natural period corresponding to the heave motion of an unmoored float is 3.25 s.

The hydrodynamic pressure acting on the standard floats are next evaluated by using hydroelastic analysis. A single unmoored float is idealized as a Mindlin plate of a flexural rigidity equivalent to that of the porous pontoon on an ideal fluid where the linear potential theory is applicable. The hybrid higher-order finite element-boundary element approach [22]; Dai et al., 2018) is employed to solve the coupled fluid-structural interaction in the frequency domain. The float is modelled as an equivalent Mindlin plate using the finite element formulation. The free-edge boundary conditions are employed such that the bending moments, torsional moments and shear forces vanish at the edge of the plate. The boundary element method is engaged for the fluid-structural interaction where the linear potential flow theory is employed. The boundary conditions for the fluid domain include the linearised kinematic and dynamic boundary conditions at the mean free surface, the body boundary conditions at the wet surface of the float, the impermeable boundary condition at the sea bed, and the Sommerfeld's radiation condition at infinity. Fig. 2 shows the hydrodynamic pressure amplitudes (Pa/m) under regular waves of unit wave amplitude A propagating along the longitudinal direction of the float. As can be seen, the highest hydrodynamic pressure amplitude occurs when the wave period is around 3 s owing to the resonance in the heave motion. For longer waves, the hydrodynamic pressure amplitude drops rapidly, which is expected as the float will follow the wave motion. Fig. 3 shows the Pierson-Moskowitz wave spectrum with significant wave height $H_s = 14$ m and peak period $T_p = 10$ s that represent an extreme sea state in an offshore condition. Also shown in Fig. 3 is the maximum hydrodynamic pressure on a float under such a harsh wave condition. The peak values are found at both front and rear parts of the float and they are shown to be less than 5.5 kPa. A preliminary finite element based structural analysis of a single float showed that such a pressure magnitude is within the allowable design pressure.

3. Model tests of a scaled array in waves

3.1. Test facility

The experimental campaign was carried out in the towing tank at the Canal de Ensayos Hidrodinámicos of the Universidad Politécnica de Madrid. The main dimensions of the tank are 100 m in length, 3.8 m in width, and 2.245 m in depth. Regular and irregular waves are generated by a single flap wavemaker placed at one end of the tank. A wave absorption beach of 8.5 m in length is located at one end of the tank (opposite side of the wavemaker). The test results are primarily used to examine the global responses of an FPV array under operational and extreme conditions.

In the model test, the Froude number is kept the same between the full- and model-scale structures and the model was downscaled by a factor (λ_s) of 60. Fig. 4 shows an isometric view of the FPV array. The dimensions of the FPV array and important physical properties are listed in Table 2. These parameters, together with descriptions of the experimental setup in Section 3.4, make it possible to establish numerical simulations under similar physical conditions. The tested material for the float is polyurethane with

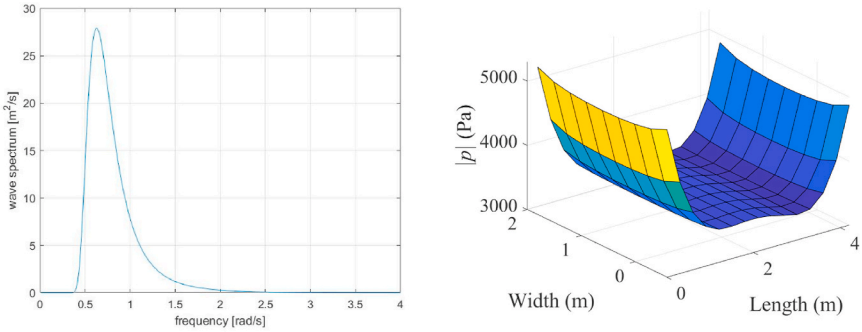

Fig. 3. Performance under harsh wave conditions: (a) Pierson-Moskowitz spectrum and (b) hydrodynamic pressure.

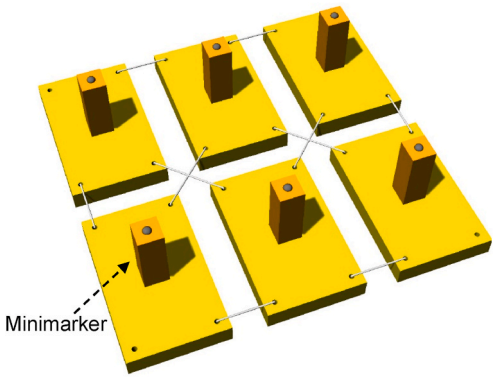

Fig. 4. Isometric view of the FPV array model with lightweight pillars and markers.

Table 2
Physical properties of the individual float and the FPV array.

Variables	Model-scale	Full-scale
Float length	78.3 mm	4.70 m
Float width	48.3 mm	2.90 m
Float height	10 mm	0.60 m
Float density (dry)	313 kg/m^3	313 kg/m^3
Float density (wet)	352 kg/m^3	352 kg/m^3
Free-floating draft (dry)	3.1 mm	0.19 m
Free-floating draft (wet)	3.5 mm	0.21 m
Array width	173.3 mm	10.4 m
Array length	178.3 mm	10.7 m
Distance between floats	16.7 mm	1.0 m
Rope density	0.5 g/m	1.8 kg/m

homogeneous mass distribution, and the material absorbs a small amount of water over time, which creates some uncertainties in the experimental results as well as for the numerical comparison. The model array with the floats is relatively lightweight compared with traditional offshore structures and the array follows the motion of the wave profile in most sea states. This characteristic makes the hydrodynamic loads of the FPV system inertia-dominated. Still, viscous drag plays a role in the presence of flow separation [23].

3.2. Model test program

Experiments in regular and irregular waves at zero forward speed were performed by following the recommendations provided by Refs. [24,25]. Table 3 and Table 4 show the test matrices implemented in regular and irregular waves. In these tables, λ refers to the wave length, H refers to the wave height, and T refers to the wave period.

The first nine regular waves (W_{R1} to W_{R9}) had periods and amplitudes typical of wind-generated ocean waves. W_{R10} represented a wave height under the survival condition. The Pierson-Moskowitz Spectrum (parameterised) was utilised for the irregular waves. W_{IRR1} and W_{IRR2} represented a standard fully developed sea, whereas W_{IRR3} described an extreme case scenario. In all the cases, the wave steepness was small, and the water depth was at least half the wavelength. However, because of the physical limitations of the wavemaker, the steepness of W_{R10} had to be increased compared to the other regular waves. A minimum of twenty wave encounter

Table 3
Test matrix for regular waves (* measured values).

ID_W	λ/L	T_M*	H*/λ	h*/λ	H_F	T_F
[−]	[−]	[s]	[%]	[−]	[m]	[s]
W_{R1}	9.1	1.00	2.0	1.37	1.9	7.8
W_{R2}	11.0	1.11	1.9	1.13	2.1	8.6
W_{R3}	13.0	1.20	2.0	0.96	2.7	9.3
W_{R4}	15.0	1.29	2.0	0.83	3.1	10.0
W_{R5}	16.9	1.37	2.0	0.74	3.4	10.6
W_{R6}	18.8	1.45	2.0	0.66	3.9	11.2
W_{R7}	20.8	1.52	2.1	0.60	4.5	11.8
W_{R8}	22.8	1.59	2.0	0.55	4.8	12.3
W_{R9}	24.7	1.66	2.0	0.50	5.1	12.8
W_{R10}	21.8	1.56	6.8	0.57	15.3	12.0

Table 4
Test matrix for irregular waves. λ, H, and T are significant values (* measured values).

ID_W	λ/L	T_M*	H*/λ	h*/λ	H_F	T_F
[−]	[−]	[s]	[−]	[−]	[m]	[s]
W_{IRR1}	6.7	0.86	1.8	1.87	1.2	6.7
W_{IRR2}	12.8	1.19	2.1	0.98	2.8	9.2
W_{IRR3}	17.9	1.41	3.9	0.70	7.2	10.9

periods were run for the regular waves, whereas the irregular waves were run for 24 min (3 h at full scale).

Fig. 5 shows two orientations implemented for the FPV array:

- 0°: the angle between the wave direction and the array is 0° (Fig. 5(a)).
- 22.5°: the angle between the wave direction and the array is 22.5° (Fig. 5(b)).

3.3. Experimental setup

Fig. 6 shows a schematic view of the setup implemented for the experimental campaign. The model was placed in the centre of the towing tank (longitudinally and transversally) to minimise wave reflection and distortion. A four-point above-water-level mooring system was utilised to prevent the model from drifting away without affecting the wave motion responses. This type of restrained system does not represent a practical mooring method, but it is commonly applied to analyse the loading and response of floating offshore platforms in the absence of catenary mooring lines (as in the present case). Light wires of linear density equal to 0.5 g/m (1.8 kg/m at full scale) of 0.9 mm diameter (5.4 cm at full scale) were utilised for the mooring lines system and the connection system between the single floats. Four holes were created on each float (2.5 mm in diameter drilled at 7.5 mm on a 45° line from each float's corner) to construct the connection system. One end of the mooring line was glued into one of the four holes, and the other end was attached to the towing tank structure by a spring connected to a Bosch Aluminium Profile through a load cell. The internal connection between floats was of a diagonal type, whereas the external connection was straight (see Fig. 4).

The load cells were HBM U9C miniature force transducers with a capacity of 200 N and an accuracy class of 0.2. The connection between the load cells and the compute was made through the data acquisition system SPIDER 8. The utilised equipment provided a force measurement resolution of approximately 1.2 g. The spring stiffness was selected to have realistic restoring characteristics of the mooring lines. Specifically, the spring stiffness was 0.95 N/m (3.43 kN/m at full scale). The spring length was determined to ensure that the spring could expand and contract without causing slacking (length of the spring shorter than its neutral length) under typical sea state conditions. The implementation of lightweight mooring lines in combination with the four-point above-water-level mooring system avoided any static deformation angle of the springs (Wan et al., 2015). The mooring lines were pretensioned to mimic a realistic catenary mooring system. Precisely, the target pretension for each mooring line was set equal to 25 g (53 kN at full scale). This pretension was determined after a numerical screening study carried out in OrcaFlex. A pulley attached at the bottom of the Bosch profile separated the mooring line into a quasi-horizontal part (between the model and the pulley) and a vertical part (between the pulley and the spring). A completely horizontal mooring line system was not implemented to avoid the pulleys getting into direct contact with the free surface wave elevation. The angle between the quasi-horizontal mooring line and the free surface was approximately equal to four degrees. The quasi-horizontal mooring lines created a 45-degree diagonal with the model float's corner.

The motions of the model were recorded with the optical tracking tool OPTITRACK-Flex 13. This system captures the movements of the model using marker-based optical tracking cameras. The number of cameras, four, was determined by considering the working space dimensions and possible obstructions. The cameras have a 1280 × 1024 (1.3 Megapixels) image resolution with a maximum frame rate of 120 frames per second. The tracked objects were passive semi-spherical retro-reflective mini-markers of 4.3 mm in

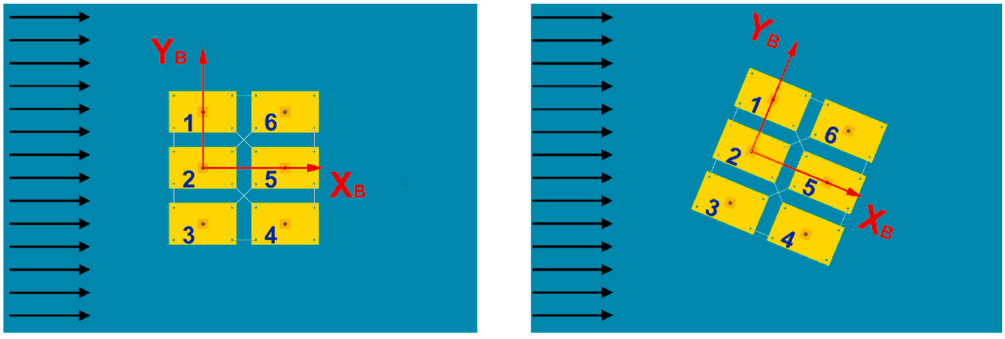

Fig. 5. Two configurations implemented for the solar array with the body-fixed coordinate system: (a) 0°, and (b) 22.5°.

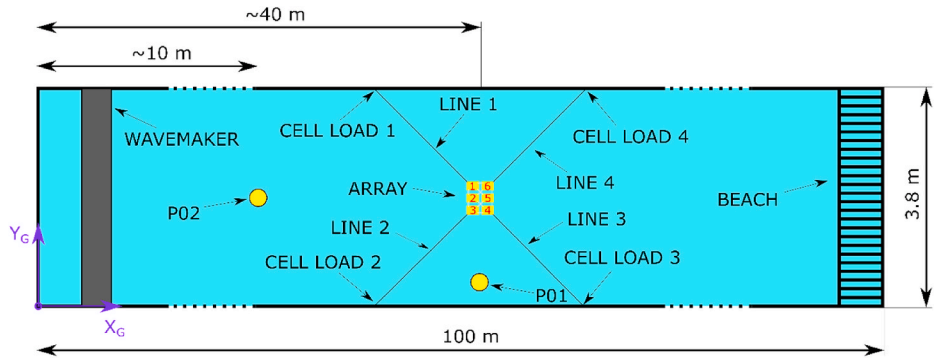

Fig. 6. Schematic representation of the experimental setup (0°) with the space-fixed coordinate system.

diameter and 0.038 g (approximately 0.29% of the float weight in wet conditions). One mini-marker was placed for each array float, leading to six mini-markers placed on the array. The mini-markers were positioned on top of lightweight pillars of $1.2 \times 1.2 \times 3.4$ cm and 0.15 g (approximately 1% of the float weight in wet conditions) glued in the middle of the array floats. This simple solution was necessary to prevent possible reflection issues caused by the water flowing onto the float. A unique rigid body (undeformable tracked object) was not created for the solar array. Instead, the mini-markers were considered individually to capture the motions of the single floats. Consequently, only translational motions of the floats were measured. The camera calibration was performed immediately before the testing with an overall reprojection 3D error of 0.5 mm.

The wave calibration was performed without the presence of the model to ensure the accuracy of the generated waves. Two

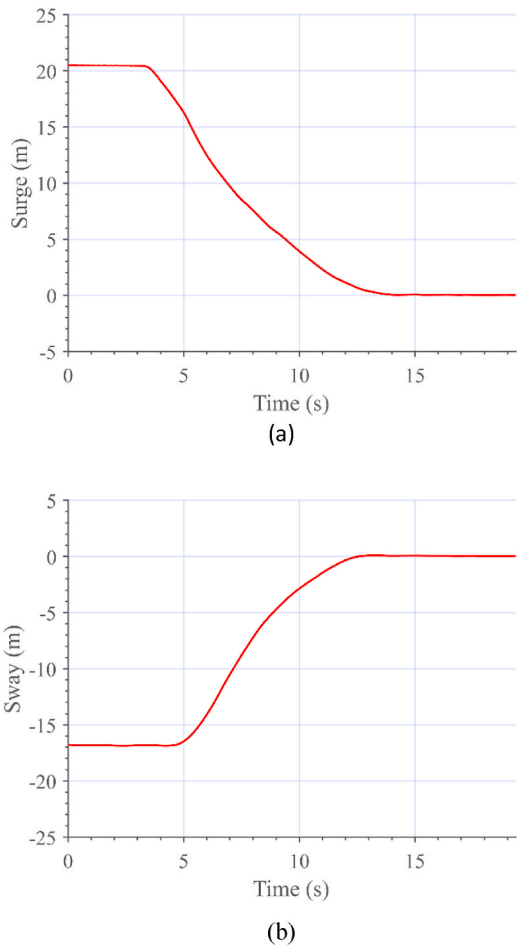

Fig. 7. Calm water decay tests (full-scale) for the complete mooring system: (a) surge and (b) sway of float 1.

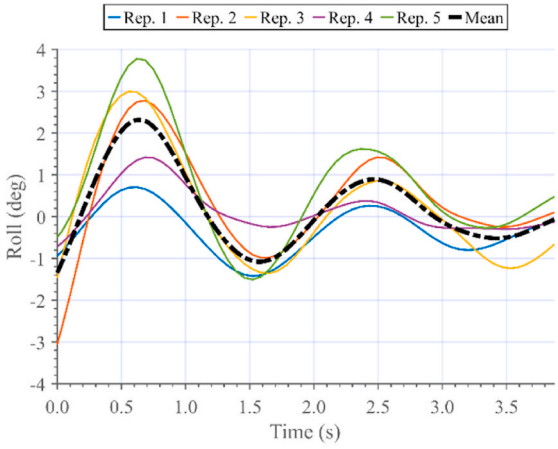

(a)

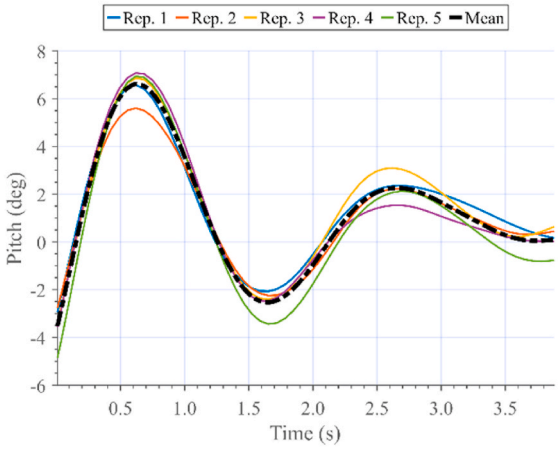

(b)

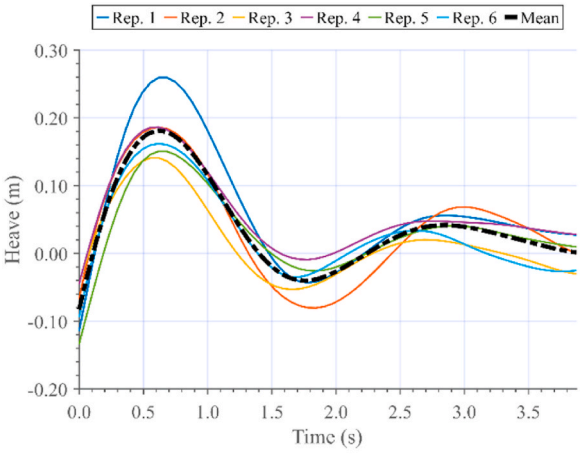

(c)

Fig. 8. Calm water free-decay tests (full-scale) for the single float: (a) roll, (b) pitch and (c) heave. High-frequency noise is removed.

capacitive wave probes were utilised to monitor the waves along the travel path. The position of the wave probes was selected to achieve fully formed waves and reduce as much as possible the impact of the array on the measurements. Precisely, one wave probe (P01) was placed between the model and the towing tank walls (at the longitudinal resting position of the array), and the other one (P02) was located at roughly 10 m in front of the wavemaker. The wavemaker flap motion was also recorded. The minimum waiting time between consecutive runs was fixed to 30 min to produce consistent results and obtain comparable conditions for each run. The water level was regularly adjusted to keep a constant value during the experimental campaign. Before running a wave test, data acquisition was conducted in calm water with the measurements from all channels. This procedure recorded the "zero" levels for all the instrumentation, which was necessary to avoid zero-drifting related issues.

3.4. Coordinate system

A body-fixed Cartesian coordinate system (see Fig. 5) and a ~~A~~ space-fixed (see Fig. 6) were employed for the experiments in waves. The space-fixed coordinate system's origin coincides with the bottom-left corner of the towing tank, whereas the body-fixed coordinate system's origin is in the middle of float 2.

3.5. Decay tests

Calm water surge and sway decay tests with the complete mooring system were conducted for the entire array. Calm water heave, pitch, and roll free-decay tests were performed for the single float. The motions were recorded with the same approach described in Section 3.3. The tests were performed by applying a prescribed displacement in the motion mode. The decay tests were repeated several times to reduce uncertainties in the results.

4. Results from the model tests

In this section, selected motion and structural response results are converted to full scale and presented for the decay, regular-wave, and irregular-wave tests. In addition, time-domain numerical simulations were carried out in OrcaFlex [26] for the extreme wave condition (W_{R10}) and the response amplitude operators (RAOs) are presented. The numerical modelling is only briefly described below due to the focus of this paper.

4.1. Decay tests

The calm water decay tests with the complete mooring system revealed that the array was overdamped both in surge and sway and underdamped in heave, roll, and pitch. Only a couple of oscillations were detected for the free-decay tests for the single float. Fig. 7 (a)-(b) show the results of the calm water decay tests at full scale with the complete mooring system in surge and sway directions, respectively. Fig. 8 (a)-(c) present the results of the calm water free-decay tests at full scale for the single in roll, pitch, and heave direction respectively. All the results are shown only for one representative float since, in all the calm water decay tests, negligible relative motions were noticed between the floats. The full-scale natural periods T_Z and nondimensional damping coefficients k, averaged over the range of the repeated free-decay tests, can be seen in Table 5. The nondimensional damping coefficients are computed as follows:

$$k = \frac{1}{2\pi} \ln\left\{\frac{z(t)}{z(t+T_Z)}\right\} \tag{5}$$

where $z(t)$ is the first crest value and $z(t+T_Z)$ is the crest value after one period.

4.2. Regular wave tests

The regular wave results focus on RAOs and time series of the float motion and mooring tension of the FPV array. As RAOs are linear transfer functions of a rigid body, it is usually inappropriate to use RAOs to understand the dynamics of a multibody system like an FPV array. Here, as negligible differences in the surge and heave motions were observed between the individual floats of the array, we still calculated RAOs for the array, but the motion RAOs should be interpreted in an average sense.

The dimensionless heave and surge response amplitude operators, RAO_H and RAO_S, were computed as the ratio between the measured response amplitudes, Y_H and Y_S, and the measured wave amplitude ζ_A. The tension response amplitude operator, RAO_T, was

Table 5
Averaged natural periods and damping coefficients in full-scale for a single float.

Degree of freedom	T_Z (s)	k (−)
Heave	2.19	23%
Pitch	2.03	17%
Roll	1.78	14%

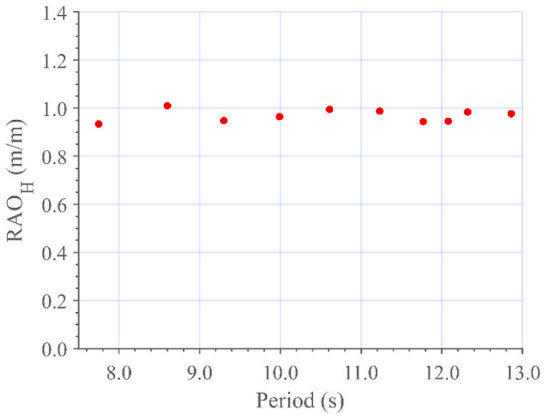

(a)

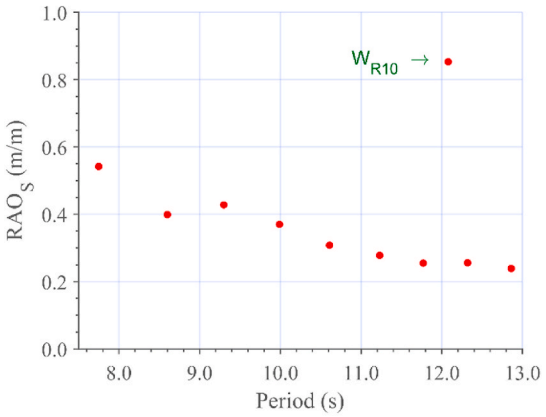

(b)

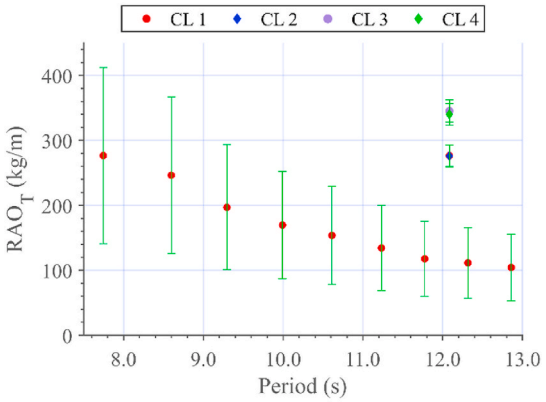

(c)

Fig. 9. (a) Heave, (b) surge, and (c) tension RAOs at full scale under regular waves for the 0° configuration. The tension RAO includes error bars based on the force measurement resolution.

calculated as the ratio between the measured response amplitude Y_T and the measured wave amplitude ζ_A.

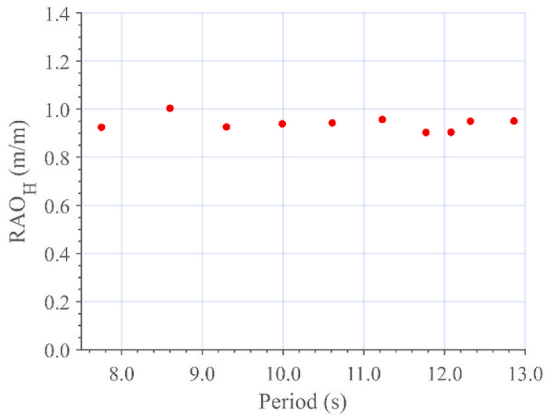

(a)

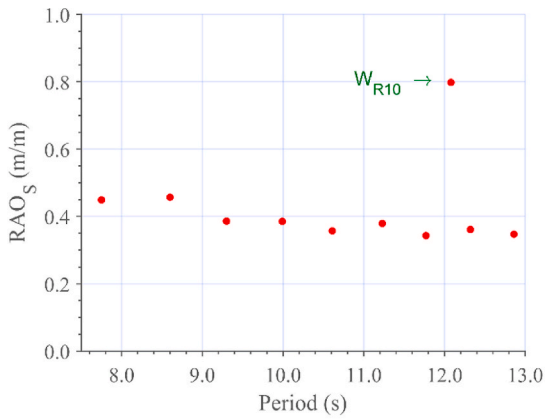

(b)

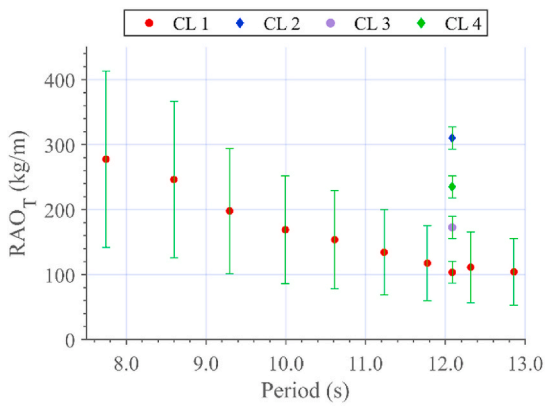

(c)

Fig. 10. (a) Heave, (b) surge and (c) tension RAOs (full-scale) under regular waves for 22.5° configuration. The tension RAO includes error bars based on the force measurement resolution.

$$RAO_H = \frac{Y_H}{\zeta_A}$$
$$RAO_S = \frac{Y_S}{\zeta_A} \quad (6)$$
$$RAO_T = \frac{Y_T}{\zeta_A}$$

Fig. 9 (a)-(c) respectively display the averaged RAO_H, RAO_S, and RAO_T of the six floats for the 0° configuration. A 10 Hz low-pass filter was applied to the surge and heave time series to remove high-frequency noises. Fig. 9 (a) shows that the heave RAO is approximately unity for all the cases. A good agreement between the numerical and experimental results for the survival condition (WR_{10}) can also be appreciated. This observation is expected since all the considered regular waves are much larger than the length of the solar array (minimum λ/L is 9.1). The surge RAO (see Fig. 9(b)) is less than one and decreases as the wave period increases. This surge RAO is different from that of other floating structures, *e.g.*, spar [27], that have a resonant peak exceeding unity. The observed trend relates to the increased restraint effect caused by the mooring system in the surge direction under long waves. The relatively low RAO magnitude is also due to viscous effects. RAOs also appear to be minimally affected by the FPV array's configuration. Furthermore, a strong nonlinearity in the surge RAO can be noticed for WR_{10}. This can be explained by the nonlinear behaviour of the mooring line tension that usually occurs for high sea states [28]. In the model test of this sea state, the mooring lines also experience substantial vibrations in both the horizontal and vertical planes. For a large FPV array with many floats, increased viscous forces are expected and the surge RAO of individual floats can be different.

The tension amplitude measured by the four cell loads was identical for the first nine regular waves (all with standard periods and amplitudes of wind-generated ocean waves). This result is caused by the small dimensions of the solar array model (scale factor $\lambda = 60$) combined with the force measurement resolution of the utilised experimental equipment (1.2 g). Based on this, error bars based on the force measurement resolution (±0.6 g) are included in the tension RAOs shown in Fig. 9. As expected, the general trend of the tension RAO resembles the surge RAO. Noticeable differences in RAO_T between the four cell loads were noticed for the wave height survival condition W_{R10}. Specifically, the tension amplitude measured by cell loads 3 and 4 were larger than the one recorded by cell loads 1 and 2 for the 0° configuration (see Fig. 5(a)). Furthermore, RAO_T for cell load 3 is comparable to that for cell load 4, and the tension amplitude measured by cell load 2 was similar to that by cell load 1.

Fig. 10 (a)-(c) respectively show RAO_H, RAO_S, and RAO_T for the 22.5° configuration (see Fig. 5 (b)). Here, surge refer to the float body-fixed coordinate system in the X_B-direction (see Fig. 5). For this misaligned wave heading, the observations for RAO_H are similar to those presented for the 0-deg wave heading. The heave RAO magnitude is approximately one regardless of the wave conditions. Because of this wave misalignment, the surge RAO magnitude, RAOs, becomes less sensitive to the wave conditions and only exhibits a minor decrease as the wave period and height increases, as shown in Fig. 10 (b).

Cell load 4 measured the largest tension amplitude for the 22.5° configuration. In comparison, the smallest RAO_T was found for cell load 1, where the strong nonlinearity disappeared.

To understand the array's behaviour in the extreme condition, W_{R10}, we also performed numerical simulations of the array in OrcaFlex. The numerical model of the FPV array resembles the downscaled physical model used in the wave tank. For each float, the hydrostatic stiffness in roll and pitch was modelled by attaching buoyancy elements to the corners. The hydrodynamic load was modelled using Morison's equation with quadratic damping. The hydrodynamic added mass coefficients in Morison's equation were obtained from the potential-flow analysis. The mooring lines were modelled with weight, drag, and added mass, but no bending stiffness was considered. The numerical model was simplified as the hydrodynamic interaction was not considered. To calibrate the numerical model, we simulated the free decay test of a single float in calm water and tuned the quadratic damping coefficient such that the simulated time series matched that of the model test. Then, the damping coefficient was further applied in the regular wave simulations.

Selected results of the heave, surge, and mooring tension RAOs for W_{R10} from the numerical model and from the model tests are summarised in Table 6 and Table 7, respectively. The motion RAOs should be interpreted in an average sense. In general, the numerically simulated motion responses follow the original time series, and a decent comparison of the RAO magnitude is observed for both wave headings. However, both the numerically obtained motion and tension transfer functions are much lower than those from the experiments. This can be explained by the fact that the numerical model is simplified and overdamped compared to the physical model. As the FPV array rides the waves and follows the wave motions in the wave condition with a long wavelength, flow separation and viscous damping of the FPV components are limited based on an analysis of the hydrodynamic load components. Due to the scope of this paper, we did not make attempts to further calibrate the numerical model.

To illustrate the dynamics of the FPV array under different wave conditions, we select two sea states, WR_5 (operational condition), and WR_{10} (survival condition) and present the response time series in Figs. 11–18.

For each wave heading and sea state, the presented motion response variables include the heave and surge motion of the individual

Table 6
Comparison of the motion RAOs of the array between numerical simulations and model tests for WR_{10}.

	Numerical results		Experimental results	
Heading	RAO_S (m/m)	RAO_H (m/m)	RAO_S (m/m)	RAO_H (m/m)
0°	0.763	1.004	0.853	0.946
22.5°	0.652	1.009	0.798	0.904

Table 7
Comparison of the mooring tension RAOs of the array between numerical simulations and model tests for WR_{10}.

	Numerically obtained RAO_T (kg/m)				Experimentally obtained RAO_T (kg/m)			
Heading	CL_1	CL_2	CL_3	CL_4	CL_1	CL_2	CL_3	CL_4
0°	178.2	178.2	207.4	207.4	276.4	275.8	345.3	340.1
22.5°	81.4	280.8	117.7	248.4	103.6	310.3	172.6	235.3

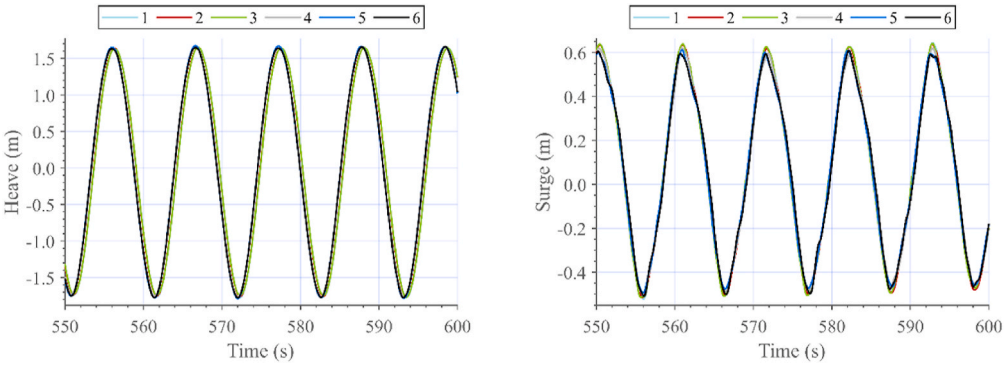

Fig. 11. Wave: W_{R5} – Heading: 0° - Time-series: heave (left) and surge (right). High-frequency noise is removed.

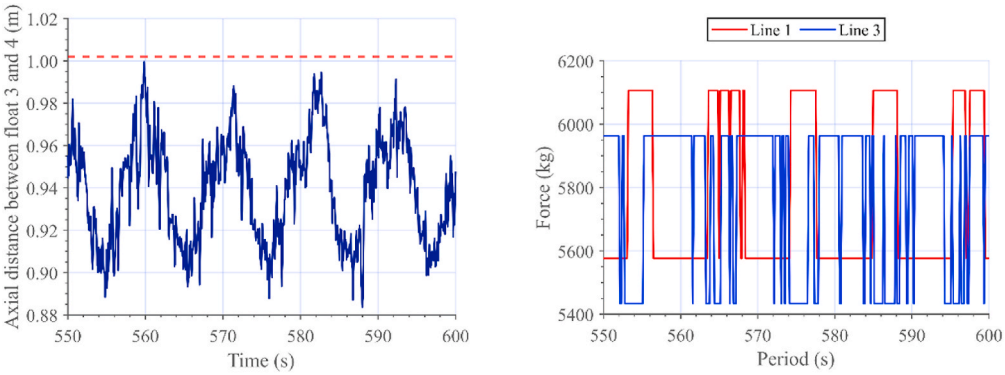

Fig. 12. Wave: W_{R5} – Heading: 0° - Time-series: relative distance between floats 3 and 4 (left) and tension (right).

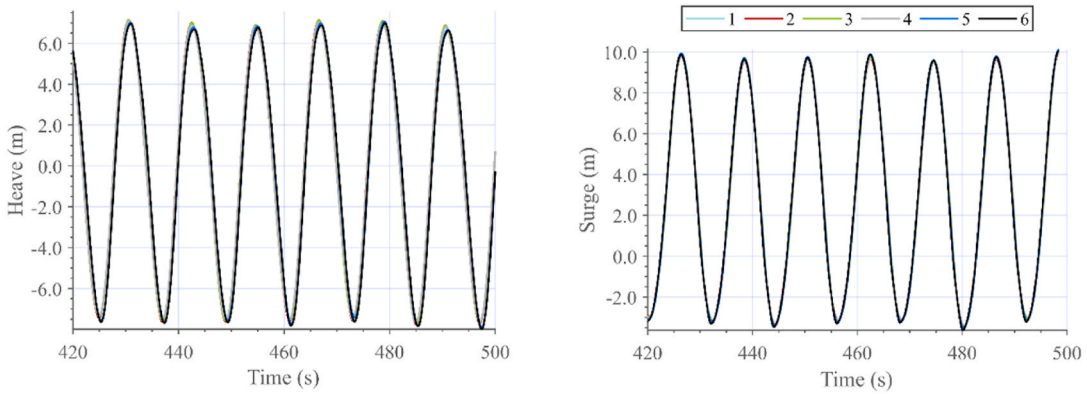

Fig. 13. Wave: W_{R10} – Heading: 0° - Time-series: heave (left) and surge (right). High-frequency noise is removed.

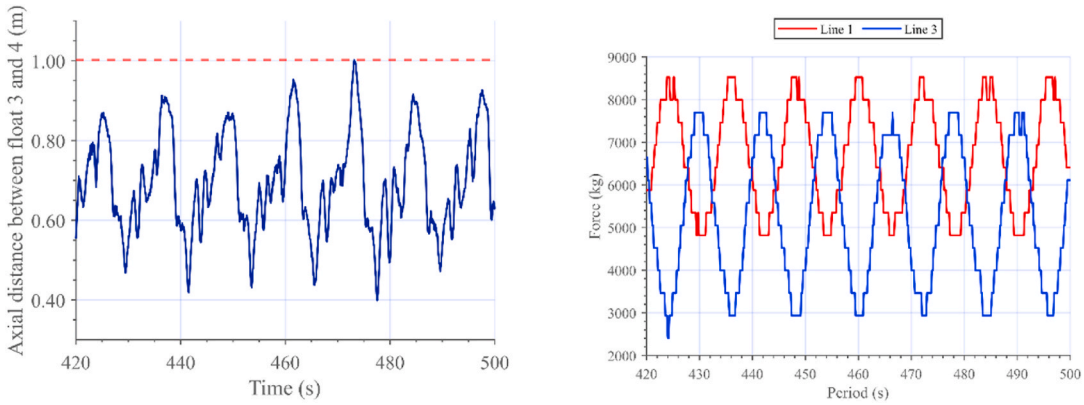

Fig. 14. Wave: W_{R10} – Heading: 0° - Time-series: relative distance between floats 3 and 4 (left) and tension (right).

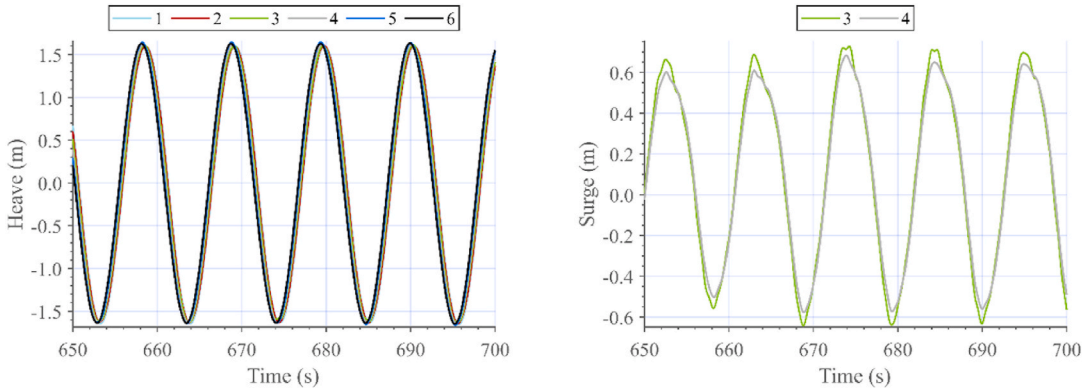

Fig. 15. Wave: W_{R5} – Heading: 22.5° - Time-series: heave (left) and surge (right). High-frequency noise is removed.

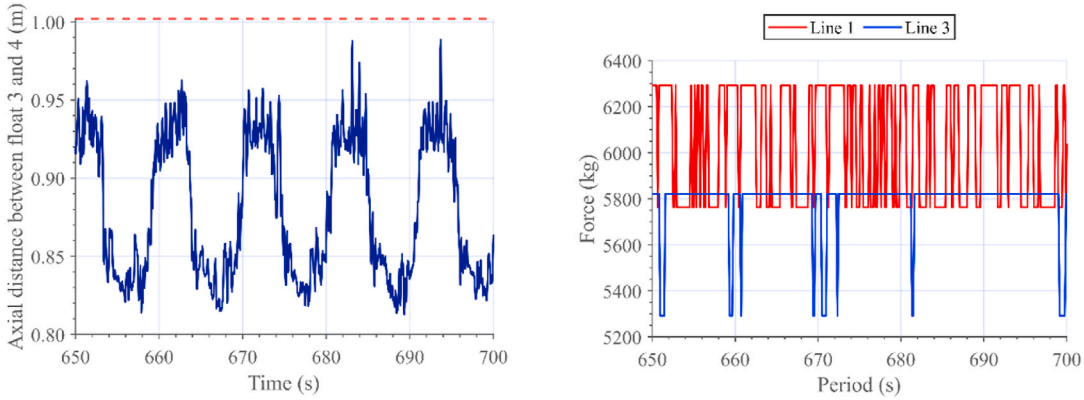

Fig. 16. Wave: W_{R5} – Heading: 22.5° - Time-series: relative distance between floats 3 and 4 (left) and tension (right).

floats, the relative horizontal distance between two adjacent floats (floats 3 and 4), and the mooring tension. Among the motion variables, the heave motion exhibits the best sinusoidal regularity in both sea states and wave headings. The heave motions of individual floats are less affected by the mooring lines and are almost following the waves simultaneously. This observation can explain the RAO magnitude. Compared with the heave motion, the surge motion follows a general trend of sinusoidal curves with uneven peaks and valleys, and the time series is not very smooth.

In the design concept, the floats are connected via ropes, and the relative distance (axial) between two floats is an important indicator of the motion characteristics of the design. As shown in Fig. 12, this relative distance generally follows a sinusoidal pattern in regular waves but exhibits many more fluctuations than the surge or heave motions. Despite the variations in the patterns, the relative

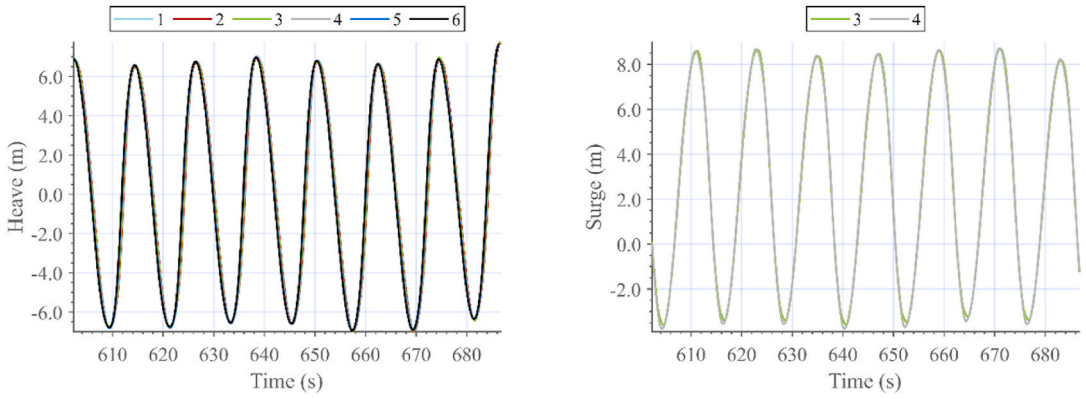

Fig. 17. Wave: W_{R10} – Heading: 22.5° - Time-series: heave (left) and surge (right). High-frequency noise is removed.

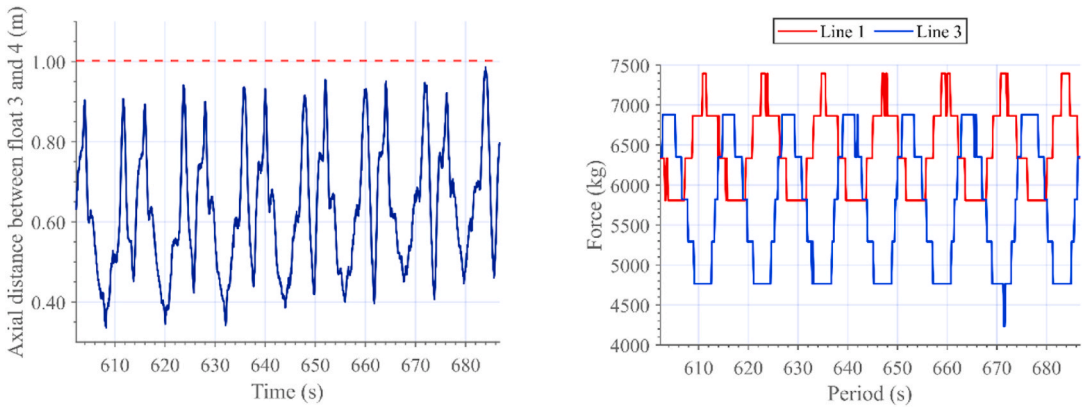

Fig. 18. Wave: W_{R10} – Heading: 22.5° - Time-series: relative distance between floats 3 and 4 (left) and tension (right).

distance is less than 1 m and remains positive in both the operational (see Fig. 12) and the survival conditions (see Fig. 14). This indicates that the neighbouring floats are not in contact with each other because of the applied pretension in the connecting ropes. Although the rope tension was not measured in the model test, this measurement can be considered in the future.

As shown in Figs. 12, 14, 16 and 18, the time series of the mooring line tensions shows a jagged shape. Especially in the operational condition, the force time series is alternating between two values. This result is due to the limitation of a 1.2g force measurement resolution applied in the model test. The actual mooring tension time series is continuous.

Comparing the two wave headings for a given sea state, we observe that the relative distance between floats 3 and 4 vary more significantly in the 22.5° configuration than in the 0° configuration, and the range of the relative distance can increase by approximately 60% in WR_5 and 20% in WR_{10}. This observation is interesting, as the current rope connection (with two crossed ropes) can be more prone to misaligned waves.

In addition to the float motions and mooring tensions, it is also relevant to examine potentially dangerous phenomena such as wave overtopping and slamming on the FPV array. For the first nine regular waves (all with standard periods and amplitudes of wind-generated ocean waves), wave overtopping and slamming have not occurred. There was no wave slamming for the wave height survival condition W_{R10} either, but a minimal amount of water was present on the floats facing the incoming wave. Three representative snapshots of the solar array under the wave height survival condition W_{R10} can be seen in Fig. 19. The snapshots demonstrate that the array followed the extreme waves without any collisions between the floats. Furthermore, it is possible to notice the nonlinear response of the mooring lines and the variation in the mooring line shape. This behaviour could be caused by nonlinear damping, nonlinear restoring force, nonlinear excitation force, or any combination of these.

4.3. *Irregular wave tests*

The motion and mooring tension responses of the FPV array under irregular wave conditions are next examined. Fig. 20 shows the motion response spectra of two floats (float 1 and float 6) for the 0° configuration. Note that floats 1 and 6 are purposely chosen as they represent the floats on both the weather and protected sides. Their translational motion response spectra under the three irregular wave conditions (see Table 4) are plotted. As can be seen, the motion responses of the two floats are virtually the same under all three

Fig. 19. Three snapshots of the solar array under the regular wave W_{R10}.

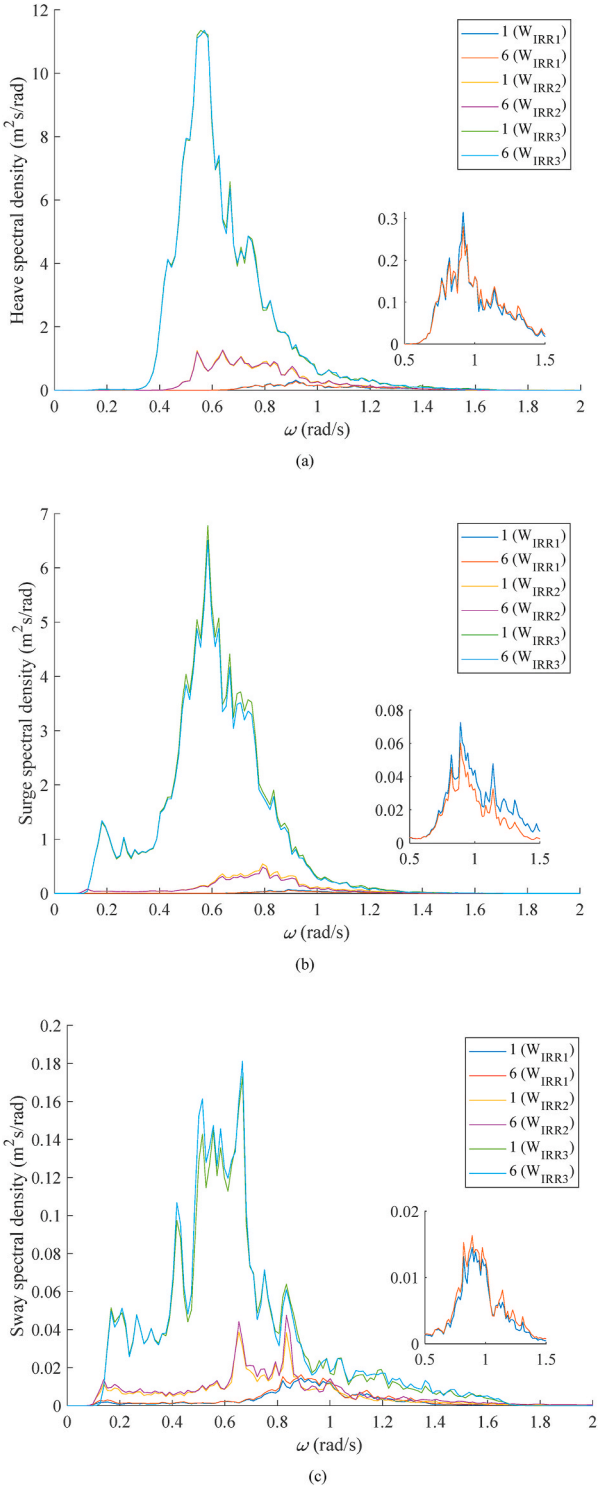

Fig. 20. Motion response spectra in heave, surge and sway for floats 1 and 6 (0° configuration). Estimation of the motion spectra is performed using the Welch method with 7000 Hamming windows and 50% overlap.

irregular wave conditions, even though float 1 is noticed to experience slightly larger responses than float 6. This indicates that the FPV array is almost transparent to incoming waves as designed such that they move along with the waves and do not absorb the huge wave energy under harsh sea states. In general, the heave motions are substantially excited around 0.6 rad/s, while the surge motions are

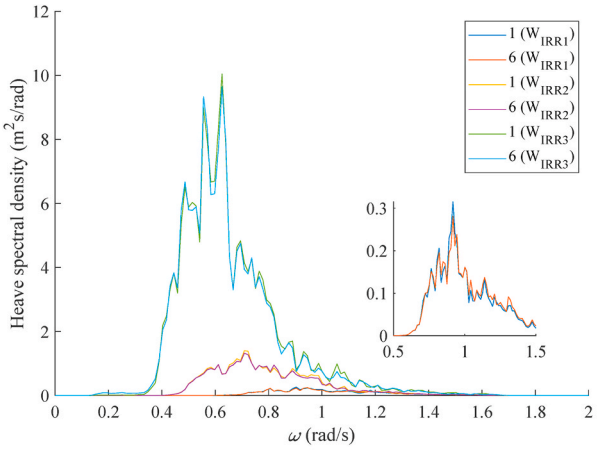

(a)

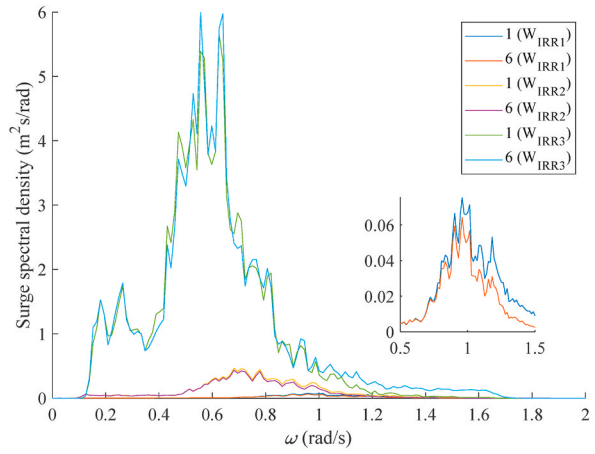

(b)

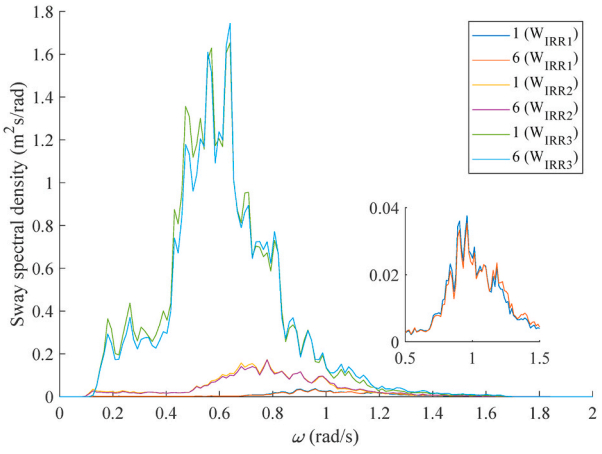

(c)

Fig. 21. Motion response spectra in heave, surge and sway for floats 1 and 6 (22.5° configuration). Estimation of the motion spectra is performed using the Welch method with 7000 Hamming windows and 50% overlap.

excited around 0.5–0.8 rad/s, particularly for W_{IRR2} and W_{IRR3}. When the FPV array is rotated by 22.5° in the horizontal plane, the motion response spectra of floats 1 and 6 are plotted in Fig. 21. Similar to that of the 0° configuration, the planar orientation does not affect the fact that the floats have virtually the same motion responses. Under this orientation, the heave, surge and sway energies are concentrated around 0.6 rad/s.

Fig. 22 shows statistics of the translational motion responses of float 1 and tension in the mooring line connecting to float 1 under irregular wave conditions. Note that the mooring tension statistics are normalized with respect to the pretenion of 53 kN. As can be seen in Fig. 22(a), the maximum heave motions are about 1 m under operational wave conditions, while they can exceed 6 m under extreme wave conditions. The planar orientation is found to have a small effect on the heave motion statistics. For the surge and sway motions, a 22.5° orientation is found to significantly increase the maximum responses, particularly for the extreme wave condition. This is in line with the observations in the regular wave tests (see Figs. 9(b) and 10(b)). If the motion along the global X_G is interested, a 64% increase in the maximum value is observed. When it comes to the mooring line tension, the effect of planar orientation of the FPV array is found to be rather small, although it introduces a slight increase in the maximum and mean values when the array is subjected to the extreme wave condition. The statistical results suggest that the 0° configuration is preferred in terms of smaller motion and tension responses under both operational and extreme wave conditions.

5. Uncertainty analysis of the model tests

Evaluating measurement errors and their possible consequences play a fundamental role in interpreting the results. The measurement error has two components: a fixed bias and a random error. The former is a systematic error that is constant during the entire experimental campaign and can be caused by installation errors of the testing model, inaccurate calibration of the equipment, inappropriate use of measurement devices, and model fabrication errors. Random errors are caused by unknown sources and unexpected changes and can be observed by repeating the measurements. In this section, the uncertainties of the model testing are discussed and, when practicable, quantified.

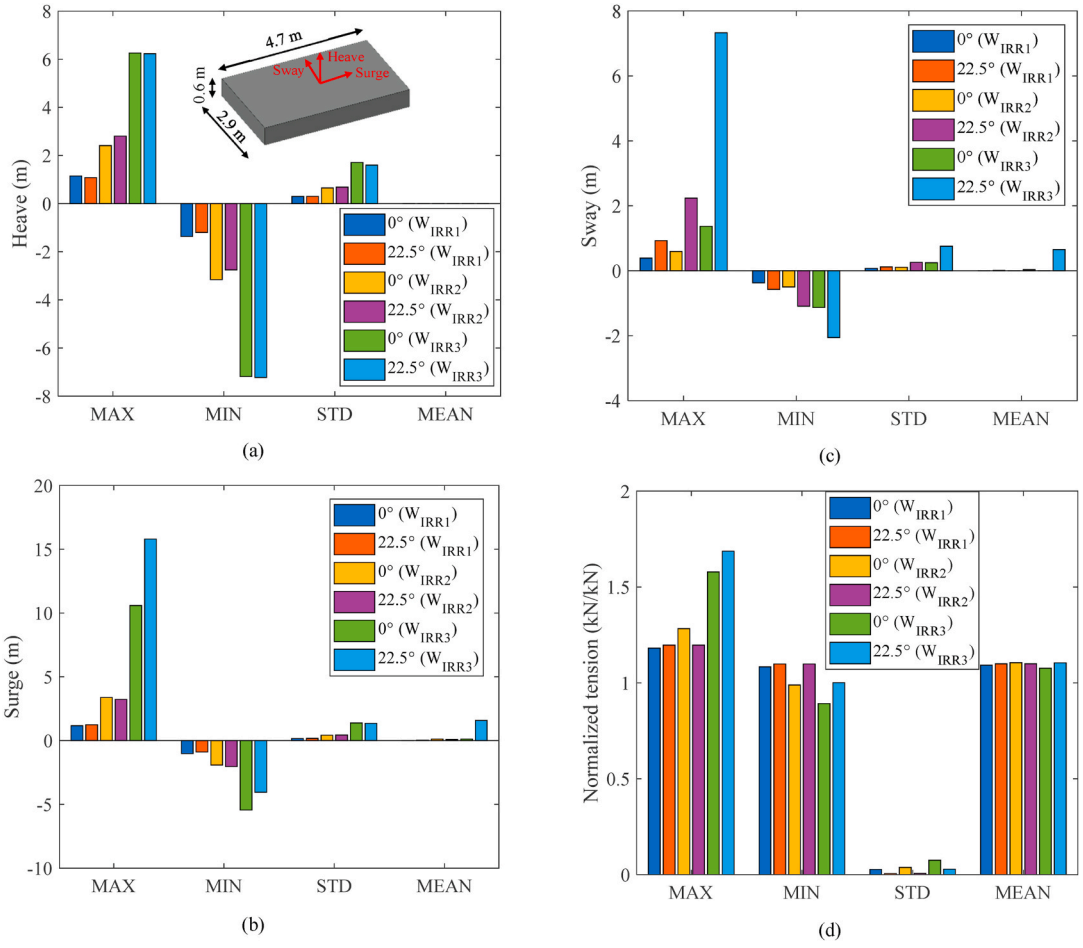

Fig. 22. Motion and tension statistics for float 1. Mooring tensions are normalized with respect to the pretension of 53 kN.

5.1. Uncertainty in model fabrication and installation

Fabrication of the model FPV array was carried out manually. A standard table saw was utilised to create the single floats. During the sawing procedures, careful examinations were applied to ensure minimal deviations between the floats. After that, all the floats were measured with a calibre, and the geometrical variations were documented: 48.3 mm ± 0.2 mm in width (2.90 m ± 1.2 cm at full scale), 78.3 mm ± 0.3 mm in length (4.70 m ± 1.8 cm at full scale), 10 mm ± 0.2 mm in height (0.60 m ± 1.2 cm at full scale). A rigid frame structure made of wood was utilised to fabricate the solar array. The frame was necessary to ensure high precision during the construction. Errors in the distance between the floats were checked with a calibre: 23.5 mm ± 0.3 mm for the diagonal connections (1.00 m ± 1.8 cm at full scale) and 1.67 mm ± 0.2 mm for the straight connections (1.41 m ± 1.2 cm at full scale). The connection between floats consisted of gluing the light wires into the floats' holes after applying enough tension to ensure a perfect horizontal connection. The target length of the mooring lines was achieved with an accuracy of ±2 mm (approximately 0.1% of the mooring line lengths).

5.2. Uncertainty in the float weight

Correctly estimating the weight of the floats is crucial to numerical modelling of the FPV array. The floats were constructed by using polyurethane. This material is highly resistant to penetration by water, but it is not entirely waterproof. This was confirmed by placing several floats in a small towing tank for seven days. The float's weight increased by approximately 12.5% compared to the dry condition. The increase in the float's volume was negligible (approximately 3–4%).

5.3. Uncertainty in the data acquisition system

The force measurement resolution is limited by the characteristics of the HBM U9C miniature force transducers combined with the features of the data acquisition system Spider 8. The former has a capacity of ±200 N with a voltage output of 0–10 V. The latter has an analog-to-digital conversion resolution of 16 bit for an input voltage span of ±10 V DC. These characteristics led to a force measurement resolution of approximately 1.2 g. This value is adequate for the typical range of forces measured in towing tank tests. Nevertheless, the large scale factor combined with mild sea states led to high uncertainties in the tension RAO.

5.4. Uncertainty in the wave generation

The regular waves generated during the tests indicated that the wave elevations were not completely stationary even under steady-state conditions but contained small fluctuations during different cycles.

On the other hand, the regular wave frequency was remarkably stable. Therefore, the wave elevation characteristics were analysed for a minimum of twenty cycles to reveal variations in the regular wave tests.

Table 8 displays the wave elevation calculated with the root mean square analysis (H*) compared to the wave elevation's standard deviations (H^*_{STD}), minimum (H^*_{MIN}), and maximum (H^*_{MAX}) values.

6. Concluding remarks

This paper presents the concept development of an innovative modular floating PV (FPV) farm for offshore conditions. Design considerations are shown for the floats, connection systems, and farm layout. Model tests of a scaled array with 3 × 2 modules and simplified geometry were performed under regular and irregular wave conditions to verify the motion performance of the system.

Table 8
Proprieties of the generated regular waves. As previously mentioned, the Pierson-Moskowitz Spectrum [21] was selected for the irregular waves. However, it was impossible to reproduce the same type of spectrum even though an extensive calibration process was performed. Fig. 23 shows the measured spectra for W_{IRR2} and W_{IRR3} against their theoretical ones. The measured spectra were determined by applying the Welch method where the windows were adapted for the two wave conditions: 464 for W_{IRR2} and 663 for W_{IRR3}. It is possible to notice a good agreement in terms of significant wave height and frequency, but the shape of the spectra at low frequencies slightly diverges from the target spectra.

ID_W	H*	H^*_{STD}	H^*_{MIN}	H^*_{MAX}
[−]	[mm]	[mm]	[mm]	[mm]
W_{R1}	15.9	0.126	15.7	16.2
W_{R2}	17.9	0.145	17.4	18.2
W_{R3}	22.4	0.153	22.0	22.9
W_{R4}	26.1	0.252	25.3	26.7
W_{R5}	28.7	0.094	27.5	29.8
W_{R6}	32.8	0.261	31.9	33.7
W_{R7}	37.5	0.252	36.2	38.4
W_{R8}	39.6	0.432	38.0	41.4
W_{R9}	42.3	0.081	40.9	43.7
W_{R10}	127.7	0.441	123.4	131.5

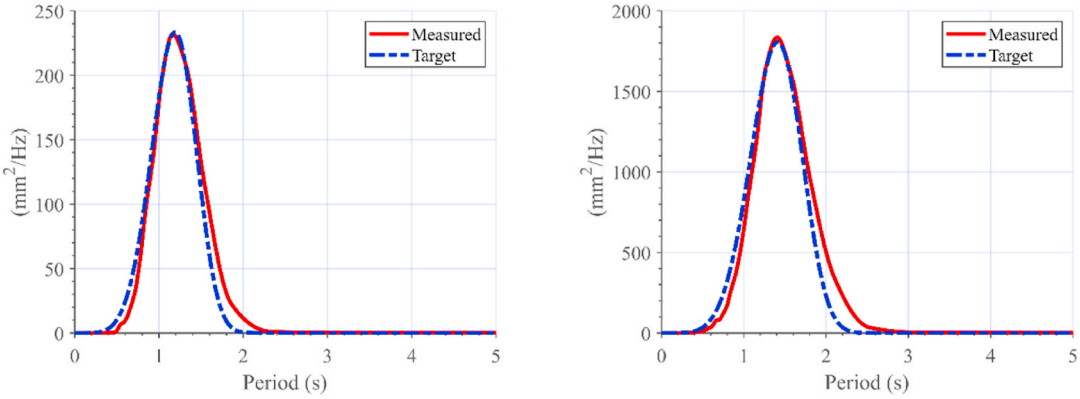

Fig. 23. Comparison between the wave spectrum for W_{IRR2} (left) and W_{IRR3} (right) with their theoretical spectrum.

From the model test results, the following key observations are made:

o The proposed FPV array exhibits excellent motion performances under both operational and extreme wave conditions. In the tested sea states, neighbouring modules did not collide with each other due to the selected rope connection and the array is able to follow the waves with limited wave overtopping.
o Although the studied array is a multibody system with 36 DOFs (6-DOF rigid body motion for each module), only a marginal difference exists for the response amplitude operator (RAO) between the modules because of the tight rope connection. Thus, an averaged RAO can be used to represent the linear motion operator of the whole array. The heave and surge RAOs vary slightly under different wave periods for a given wave steepness of 2.0, but a large surge RAO is observed under the extreme sea state because of the system nonlinearities.
o Analysis of the motion spectra and of the FPV array under three irregular wave conditions and two wave headings show that the motion spectra of float 1 and float 6 are very similar to each other.
o Response statistics of one selected float's heave, surge, and sway motion and mooring tension reveal that the two studied array orientations (22.5° versus 0°) has relatively small effects on the extreme heave motion and mooring tensions, but more significant effects on the extreme surge and sway motions. The 0-degree orientation is observed to perform bettern in terms of smaller extreme motion responses and mooring tensions in this study.
o Because of the unconventional model test setup and material use, there are various sources of uncertainties affecting the results. The identified sources of uncertainty include the fabrication and assembly of the model FPV array, the float weight, the data acquisition system used to measure the mooring tension, and the wave generation. Among these sources, the data acquisition is regarded as a major limitation because of the large scaling factor and hence the high precision requirement for the mooring system of the solar array.

7. Limitations and future work

This work is preliminary and limited to a conceptual design with experimental investigations of a downscaled small array. In the future, the technical feasibility of the design concept remains to be further improved by considering wave tank tests of a larger array, choice of recyclable composite materials with higher strength and durability, integration of the system components including mooring and anchors, and evaluating the energy performance of the array in operational conditions. The economic feasibility should be demonstrated by benchmarking the lifecycle costs against those of other offshore FPV concepts.

Declaration of competing interest

The authors declare that they have no known competing financial interests or personal relationships that could have appeared to influence the work reported in this paper.

Data availability

Data will be made available on request.

Acknowledgements

The first author and second author acknowledge the Support for Project Establishment and Positioning (PES) received from the Research Council of Norway granted through the University of Agder and Oslo Metropolitan University, respectively. This research has

also been partially funded by the Ministry of Science, Innovation and Universities (MCIU) of Spain under the projects FOWT-DAMP2, Ref: PID2021-123437OB-C21 and FOWT-PLATE-MOOR, Ref TED2021-130951B-I00. The authors are grateful to Kasper Sandal (cDynamics AS) and Julie Teuwen (TU Delft) for valuable discussions on the concept development.

References

[1] Conti J, Holtberg P, Diefenderfer J, LaRose A, Turnure JT, Westfall L. International energy outlook 2016 with projections to 2040. Washington, DC, United States: USDOE Energy Information Administration (EIA); 2016.
[2] Dai J, Zhang C, Lim HV, Ang KK, Qian XJ, Wong JLH, Tan ST, Wang SL. Design and construction of floating modular photovoltaic system for water reservoirs. Energy 2020;191:116549.
[3] Oliveira-Pinto S, Stokkermans J. Assessment of the potential of different floating solar technologies–overview and analysis of different case studies. Energy Convers Manag 2020;211:112747.
[4] Liu H, Krishna V, Lun Leung J, Reindl T, Zhao L. Field experience and performance analysis of floating PV technologies in the tropics. Prog Photovoltaics Res Appl 2018;26(12):957–67.
[5] DNVGL. Recommended practice deisign of floating solar PV DNVGL-RP-0584. 2020.
[6] Bellini E. Offshore floating PV may reach maturity in 2030. PV Tech Power. 2020. Retrieved.
[7] Trapani K, Millar DL. The thin film flexible floating PV (T3F-PV) array: the concept and development of the prototype. Renew Energy 2014;71:43–50.
[8] Putschek M. Experiences of marine floating PV projects. Munich, Germany: Intersolar conference; 2018.
[9] Eisl R, Haider M. Heliofloat – a floating lightweight platform. 2022. Retrieved, . [Accessed 14 January 2022].
[10] Bjørneklett B. Offshore floating solar-a technical perspective. PV Tech Power 2018;16(16):6–9.
[11] Vagle S, Bjar L. Offshore floating solar panel park – a concept. Oslo, Norway: International Solar Day; 2018.
[12] Equinor ASA. Will test floating solar off Frøya. 2022. Retrieved, . [Accessed 14 January 2022].
[13] Mukdahan C. A feasibility study of entering the solar energy market: the case of heliorec. Thailand: College of Management, Mahidol University; 2019. Msc Thesis.
[14] Pereya BT, Jiang Z, Gao Z, Anderson MT, Stiesdal H. Parametric study of A counter weight suspension system for the tetraspar floating wind turbine. Proceedings of the ASME 2018 international offshore wind technical conference. San Francisco, USA: IOWTC 2018; 2018.
[15] DNVGL. Standard DNVGL-ST-0119 Floating wind turbine structures. 2018.
[16] Ditlevsen O, Madsen HO. Structural reliability methodsvol. 178. New York: Wiley; 1996.
[17] Jiang Z, Hu W, Dong W, Gao Z, Ren Z. Structural reliability analysis of wind turbines: a review. Energies 2017;10(12):2099.
[18] Turner AA, Steinke DM, Nicoll RS, Stenmark P. Comparison of taut and catenary mooring systems for finfish aquaculture. In international conference on offshore mechanics and arctic engineeringvol. 51258. American Society of Mechanical Engineers; 2018, June. V006T05A008.
[19] Liang G, Jiang Z, Merz K. Mooring analysis of a dual-spar floating wind farm with a shared line. J Offshore Mech Arctic Eng 2021;143(6).
[20] Zhang C, Wan L, Magee AR, Han M, Jin J, Ang KK, Hellan Ø. Experimental and numerical study on the hydrodynamic loads on a single floating hydrocarbon storage tank and its dynamic responses. Ocean Eng 2019;183:437–52.
[21] DNV. Recommended Practice DNV-RP-H103 modelling and analysis of marine operations. 2011.
[22] Nguyen HP, Dai J, Wang CM, Ang KK, Luong VH. Reducing hydroelastic responses of pontoon-type VLFS using vertical elastic mooring lines. Mar Struct 2018;59:251–70.
[23] Faltinsen O. Sea loads on ships and offshore structures. Cambridge university press; 1993.
[24] ITTC. Recommended procedures and guidelines: floating offshore platform experiments. In: International Towing Tank Conference, 7; 2021. p. 5. 0.2-07-03.1, 2021.
[25] ITTC. Recommended procedures and guidelines: guideline for model tests of stationary multi-bodies operating in close proximity. In: International Towing Tank Conference, 7; 2021. p. 5. 02-07-03.1.
[26] Orcina. OrcaFlex (version 11.2c) documentation. 2022.
[27] Ahn HJ, Shin H. Model test and numerical simulation of OC3 spar type floating offshore wind turbine. Int J Nav Archit Ocean Eng 2019;11(1):1–10.
[28] Xu K, Larsen K, Shao Y, Zhang M, Gao Z, Moan T. Design and comparative analysis of alternative mooring systems for floating wind turbines in shallow water with emphasis on ultimate limit state design. Ocean Eng 2021;219:108377.